chosen for the numerical experiments provided the best compromise between the model size, the computation cost and the modelling constraints, e.g. dispersion and stability criterion.

The reflection response observed in a heterogeneous layer cannot easily be explained by only one scattering mode (section 2.2). Instead, it is regarded as the superposition of specular reflection, scattering, diffraction and refraction. In the following the term *reflectivity* is referred to as the apparent reflection response recorded in the data. Note, that in general a direct extraction of reflection coefficients from the results is not the primary goal of this study.

3.2.1 Image distortion due to a heterogeneous overburden

The influence of a heterogeneous layer on the reflection image is the subject of the first experiment. The reflections from the heterogeneous layer and from the deep reflector were investigated. Thereby, the reflection strength and the shape were analysed in dependence on the magnitude of the velocity fluctuation and the correlation lengths of the heterogeneities.

Model set-up

The velocity models consisted of a 100 km wide and 80 km deep area (Fig. 3.3). The grid spacing was defined according to the dispersion criterion (section 3.1.1) and was set to $\Delta x = 25$ m and $\Delta z = 25$ m. The source wavelet had a sampling interval of $\Delta t = 0.001$ s and was implemented as an explosion point source. The dominant frequency of the wavelet was 12.5 Hz, its maximum frequency was approximately 30 Hz. The velocity models consisted of a 70 km thick upper part and a 10 km thick lower part. The background P-wave velocity of the upper part was $v_P = 6000$ ms^{-1}, the P-wave velocity of the lower part was $v_p = 8000$ ms^{-1}. The v_P/v_S ratio was set to $\sqrt{3}$. The corresponding shear velocities were $v_S = 3464$ ms^{-1} for the upper part and $v_S = 4618$ ms^{-1} for the lower one, respectively. The resulting dominant and minimum wavelengths (P-wave) were about 480 m and 150 m, respectively. The normal-incidence Fresnel zone W_{Fr} at a depth of 20 km was about $W_{Fr} \approx 2500$ - 4500 m. The densities were calculated after the empirical Nafe-Drake relation (Ludwig et al., 1970) with

$$\rho = (1.755 + 0.155 \cdot v_P \cdot 0.001) \cdot 1000 \; [kg/m^3]. \tag{3.4}$$

with the P-wave velocity v_P [m/s]. The corresponding densities of the upper and of the

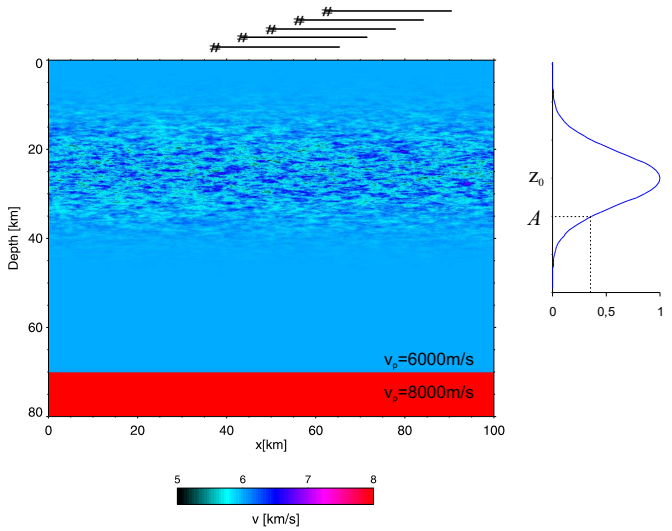

Figure 3.3: Layout of the velocity model. The heterogeneous layer was generated using an exponential autocorrelation function. The standard deviation of the velocity fluctuation is 5 %. The horizontal and the vertical correlation lengths are $a_x = 1000$ m and $a_z = 200$ m. An exponential tapering function was applied to the fluctuation field in the vertical direction. The stars and black lines on top represent the source points and receiver spreads.

lower part were $\rho_1 = 2685$ kgm^{-3} and $\rho_2 = 2995$ kgm^{-3}, respectively.

The heterogeneous layer was positioned in the upper part at depths between 10 km and 40 km. The velocity fluctuations were distributed according to an exponential autocorrelation function. The relative velocity fluctuations were calculated corresponding to the background velocity of the upper part. Instead of choosing the von-Kármán distribution (see section 2.1), which is commonly used to represent the fractal nature of heterogeneous structures in the earth, the limited frequency bandwidth of the data made the choice of an exponential autocorrelation function reasonable. The velocity fluctuations were tapered in the vertical direction. An exponential weighting function was applied to the velocity fluctuation field to avoid strong impedance contrasts at the top and the bottom of the heterogeneous layer (Fig. 3.3). The tapered velocity fluctuation field $\bar{\xi}(\vec{r})$ was calculated by

$$\bar{\xi}(\vec{r}) = \xi(\vec{r}) \cdot \exp(-\frac{(z - z_0)^2}{A^2}), \tag{3.5}$$

with the velocity fluctuation field $\xi(\vec{r})$ and the depth z. The weighting function equals 1 at the depth z_0. The function decreases exponentially with increasing distance from z_0. It becomes $\frac{1}{e}$ when the vertical distance to z_0 is $A = \mid z - z_0 \mid$. In all models z_0 and A were set

to 25 km and 15 km, respectively. The density was kept constant with $\rho_1 = 2685$ kgm^{-3}.

Twelve models with varying standard deviation and horizontal correlation lengths were calculated (Fig. 3.4). The vertical correlation length was kept constant ($a_z = 200$ m) in all models. The horizontal correlation lengths were set to 1000 m, 4000 m, and 6000 m. The aspect ratios of the horizontal and the vertical correlation lengths in all models were greater than 4, referring to various values from studies of crustal structures (Holliger and Levander, 1992; Dolan et al., 1998). Thus, the heterogeneities were predominantly horizontally oriented. The standard deviations of the velocity fluctuations were 1 %, 5 %, 10 %, and 20 %, such that examples for weak, intermediate and strong scattering regimes were provided.

Five shot gathers were calculated for each velocity model using a roll-along geometry. The shot point spacing was 6.25 km. The first shot point was at $x = 37.5$ km, the last one at $x = 62.5$ km (Fig. 3.3). 252 receivers were positioned on the right-hand side of each source location. The receiver spacing was 100 m. This provided a maximum offset of 25.2 km. In Tab. 3.1, the shot and receiver locations are given. The total recording time of the shot

Shot No.	Shot location	Receiver spreads
Shot 1	37.50 km	37.60 - 62.8 km
Shot 2	43.75 km	43.85 - 69.05 km
Shot 3	50.00 km	50.10 - 75.30 km
Shot 4	56.25 km	56.35 - 81.55 km
Shot 5	62.50 km	62.6 - 87.80 km

Table 3.1: Source and receiver locations of the numerical experiments.

gathers was 30 s. Fig. 3.5 shows one synthetic seismogram section with the main recorded reflection events: The direct wave, the backscattered wave field between 5 s and 15 s two way travel time (TWT) and the P-reflection from the lower layer between 23.5 s and 24.5 s TWT. A closer look revealed that the coherency of the reflection hyperbola suffered from amplitude and phase fluctuations (zoom in Fig. 3.5). A coda with a length of 0.5 s was generated by the interaction of the propagating wave field with the heterogeneities in the medium. The synthetic shot gathers were prestack depth migrated using a constant migration velocity of $v = 6000$ ms^{-1}. Data enhancement steps, e.g. frequency filtering, geometrical spreading correction, were not applied. Phase stacking of the migrated single sections yielded the final depth sections.

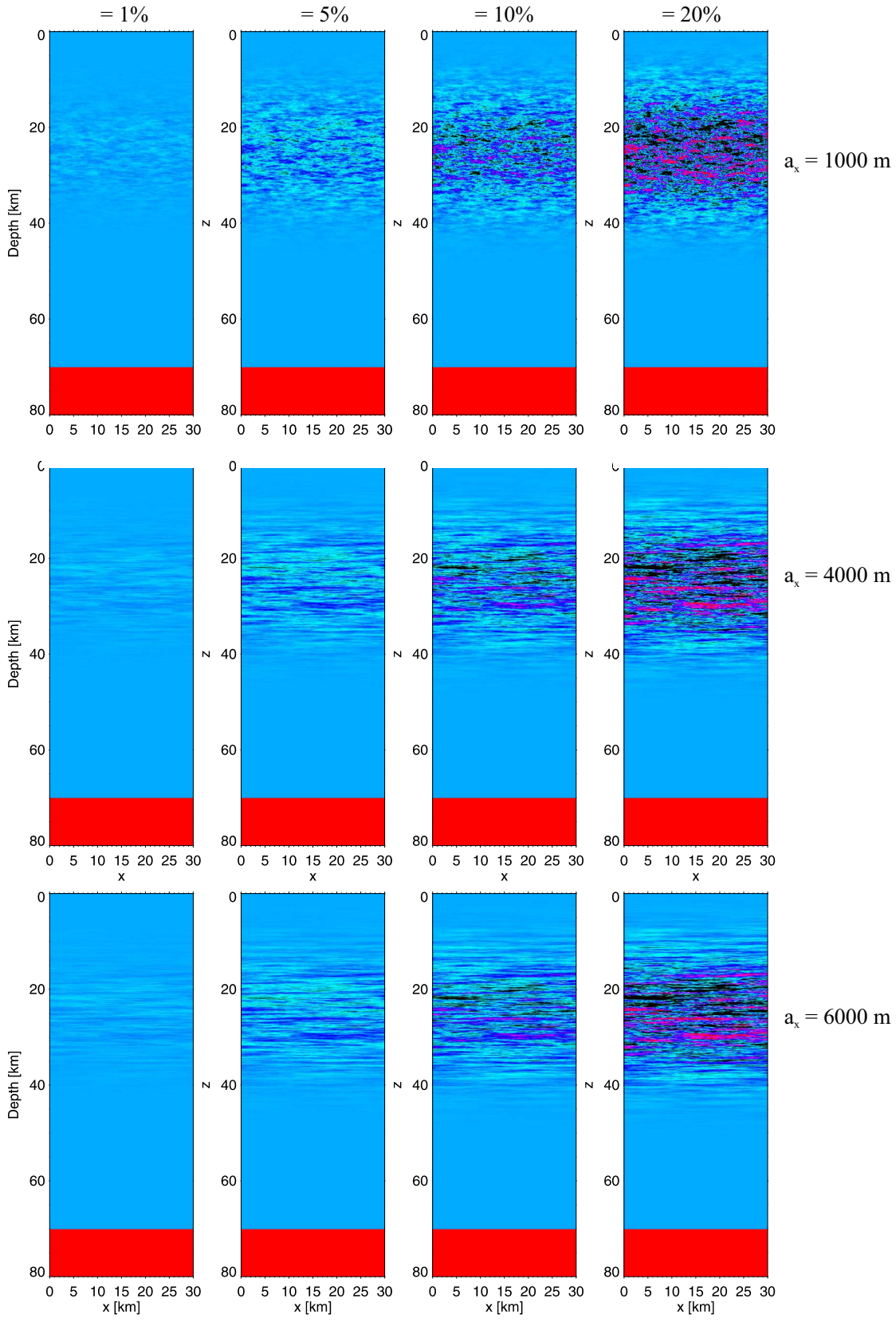

Figure 3.4: The 12 velocity models with varying standard deviations and horizontal correlation lengths. The vertical correlation length is constant ($a_z = 200$ m).

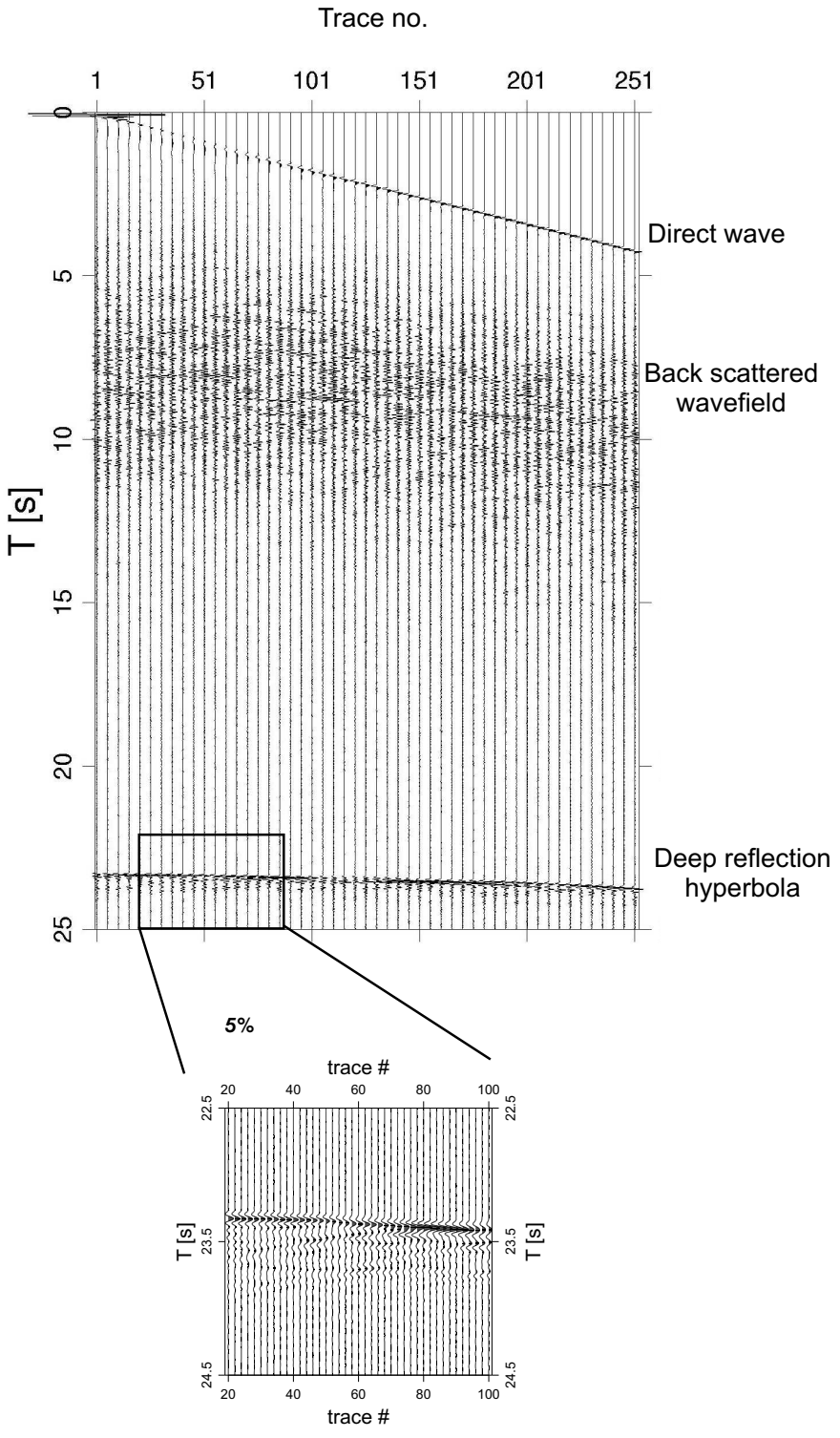

Figure 3.5: Synthetic seismogram section (vertical displacement) obtained from FD modelling (every 5th trace is displayed). The synthetic record shows a complex backscattered wave field between $5-15$ s and a deep reflection hyperbola at ≈ 23.5 s with coda wavelets. Zoom of the hyperbola shows that the recorded wave field contains amplitude and phase fluctuations.

Results

The final depth sections are shown in Fig. 3.6. The sections are displayed corresponding to the arrangement of the velocity models in Fig. 3.4. The amplitude scaling is equal for all sections. Every depth image shows a 30 km wide and 80 km deep part of the model. The focus of the reflectivity analysis is set on these regions. The apparent strong reflections at depths of about 5 km are due to the migration of the direct waves, which were not suppressed before migration.

The images show that the apparent reflectivity in the heterogeneous layer increases when velocity fluctuations become strong. Comparing the images with the same standard deviation it is observed that the reflectivity in the heterogeneous layer is stronger for large correlation lengths. For short correlation length the apparent reflectivity is weaker. The reflectivity of the deep reflector decreases with increasing standard deviation of the velocity fluctuation. For 5% standard deviation the shape of the deep reflector is more coherent for long correlation lengths than for short ones. The apparent reflectivity is of similar strength. For 10 % standard deviation the deep reflector appears discontinuous for large correlation lengths. The reflector becomes weak and almost invisible for short correlation lengths. For strong velocity fluctuations the deep reflector nearly disappears.

To quantify the change of reflectivity the average reflectivity in the heterogeneous layer and along the deep reflector was calculated. Instead of using the geometrical or the arithmetic mean, the average reflectivity R_{ave} was obtained by

$$R_{ave} = \sqrt{\frac{1}{n}\sum_{n} A_n^2}. \tag{3.6}$$

with the amplitude A of the depth traces and the number of the summed amplitudes n. The average reflectivity R_{ave} of the heterogeneous layer was calculated for a 30 km wide and 20 km deep area between $x = 35$ - 65 km and $z = 15$ - 35 km. For the deep reflector R_{ave} was calculated between $x = 35$ - 65 km and between depths of $z = 68$ - 72 km. The diagrams in Fig. 3.7 show the results. The curves are displayed in dependence on the standard deviation and the horizontal correlation length. To provide a better graphical presentation R_{ave} was normalised to the maximum in each plot.

The results show that for a standard deviation of 1 % the reflectivity in the heterogeneous layer is similarly weak for all correlation lengths. When velocity fluctuations become strong then the reflectivity in the heterogeneous layer increases. A comparison of the models with the same standard deviation but different correlation lengths shows that

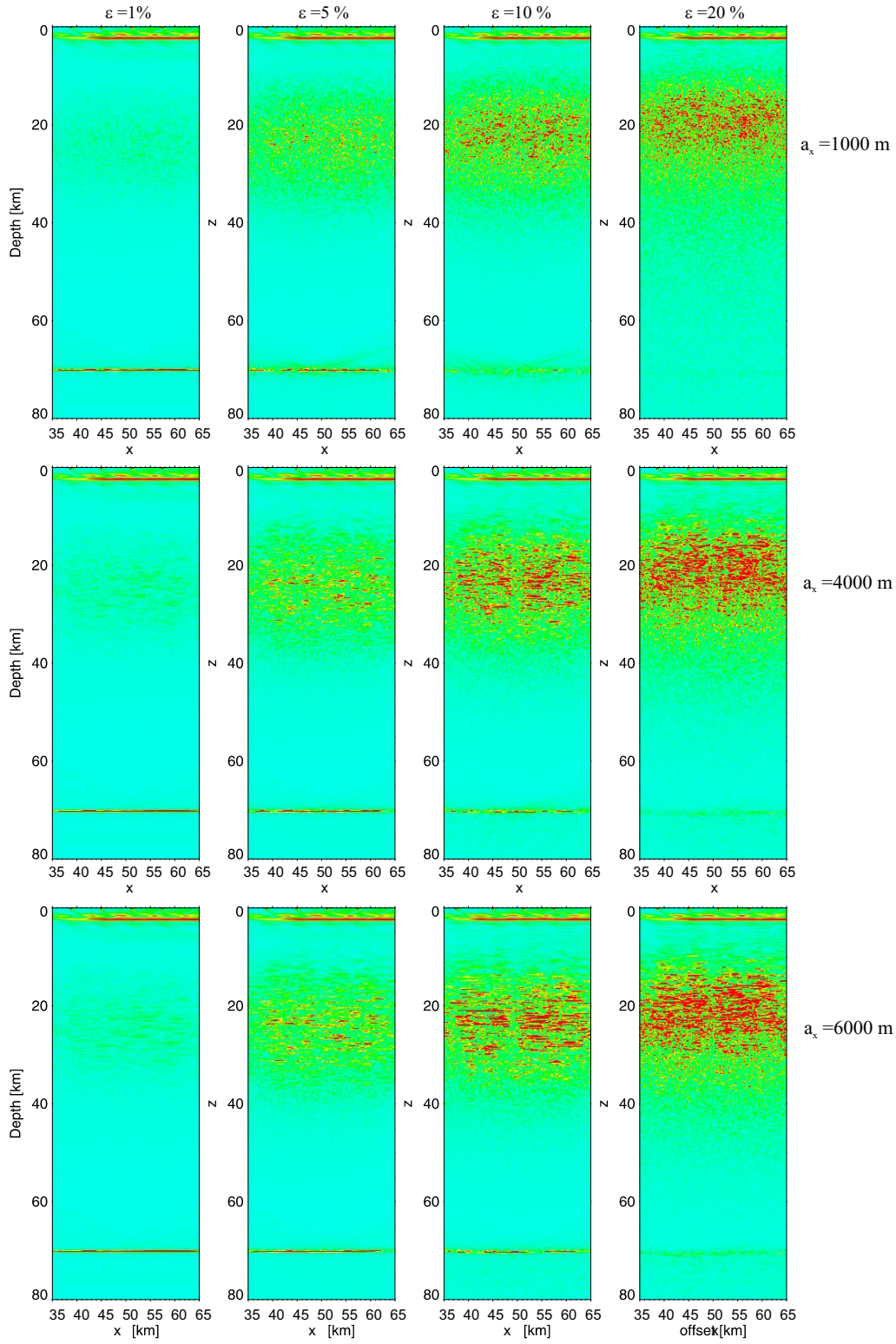

Figure 3.6: The synthetic depth sections. The reflectivity in the heterogeneous layer increases for strong velocity fluctuation. The deep reflector appears weak and discontinuous for large standard deviation and short horizontal correlation length. For a standard deviation of 20 % the deep reflector nearly disappears in all images.

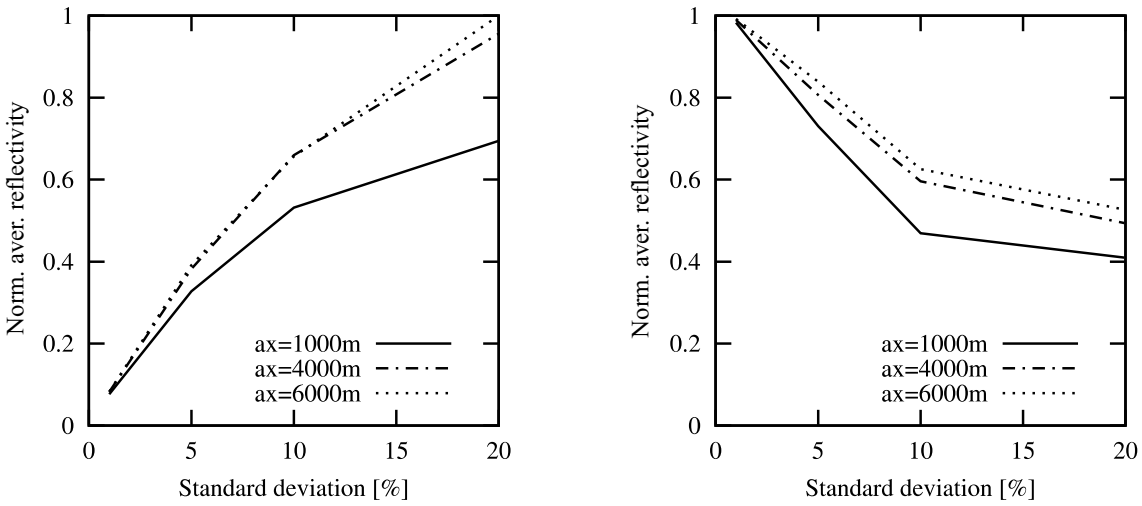

Figure 3.7: **Left**: The average reflectivity in the heterogeneous layer (solid: $a_x = 1000$ m; dashed dotted: $a_x = 4000$ m; dotted: $a_x = 6000$ m). For weak velocity fluctuations the average reflectivity is small for all correlation lengths. For larger standard deviation the reflectivity is strong for large correlation lengths. **Right**: The average reflectivity along the deep reflectors decreases for increasing standard deviation. The weakest reflectivity is observed for short correlation lengths.

the average reflectivity in the heterogeneous layer is higher for large correlation lengths than for smaller correlation lengths. The same is observed for the reflectivity of the deep reflector. For weak velocity fluctuations the average reflectivity of the deep reflector is similar for all correlation lengths. Considering the same standard deviation of the velocity fluctuation then the reflectivity is weak for small correlation lengths in comparison to the reflectivity for large correlation lengths. The observations are explained as follows. Weak reflectivity is observed for the models with a correlation length of $a_x = 1000$ m. The correlation length is of similar size to the dominant wavelength (480 m) and resonant scattering becomes dominant. The wave field is scattered in many directions and only a small part propagates back to the receivers at the surface. Thus, the amount of recorded energy is small. This leads to the observation of the apparently weak reflectivity of the heterogeneous layer. The loss of the transmitted waves becomes strong as the wave field is scattered twice in the heterogeneous layer while travelling down- und upward again. As a consequence the reflectivity of the deep reflector becomes weak. Strong reflectivity is observed for the models with the correlation lengths of $a_x = 4000$ m and $a_x = 6000$ m. There, the correlation lengths are large compared to the wavelength and forward scattering becomes dominant. The correlation lengths are of similar size to the width of the Fresnel zone. This means that mainly specular reflection as well as diffraction effects occur during

wave propagation (see Flatté et al. (1979) in section 2.2.1). The transmitted waves are less affected by energy loss such that more energy is reflected back to the surface.

The results show that the amount of scattered energy in the heterogeneous layer is not only dependent on the magnitude of the velocity fluctuation, but also on the size of the wavelength relative to the correlation length. Scattering attenuation is severe when velocity fluctuations are strong and when correlation lengths are in the order of the dominant wavelength. Consequently, the apparent reflectivity of reflector below the heterogeneous layer is strongly dependent on the latter as well. The apparent reflectivity can be significantly decreased by scattering loss when the correlation length and the wavelength are of similar size. Deep reflectors cannot be imaged and will not be detected. In real data application this might lead to structural misinterpretation of reflection images and thus should be considered.

In the following the results from numerical modelling will be compared to the results obtained from the ANCORP experiment.

Comparison of the results with the ANCORP data

The synthetic depth sections are compared to the ANCORP image introduced in chapter 1 (Fig. 3.8). In the ANCORP image it is observed that the strong Nazca reflector suddenly changes its reflectivity at depths larger than 80 km. In the poststack depth section the Nazca reflector completely disappeared (ANCORP Working Group, 1999). It is assumed that the Nazca reflector at those depths is related to a highly reflective zone above the oceanic crust rather than marking the top of the oceanic crust (ANCORP Working Group, 2003). The strong reflectivity is explained by massive dehydration of the oceanic crust, where a large amount of water is released by the eclogite transformation at the top of the crust. It is also suggested that the fluid release causes the formation of hydrous phases, e.g. serpentinite and talc, within the continental mantle wedge located above the oceanic crust. Furthermore, it is assumed that the destruction of permeability causes trapping of the ascending fluids at the mantle hydration front. This fluid rich zone in consequence causes strong impedance contrasts. In addition slab parallel shearing of the weak hydrated mantle containing fluid filled lenses and pockets is supposed to contribute to the observed high reflectivity of the Nazca reflector. Following these arguments the abrupt disappearance is explained by either the completion of dehydration of the oceanic crust or by the break down of serpentine stability due to temperature increase at larger depths.

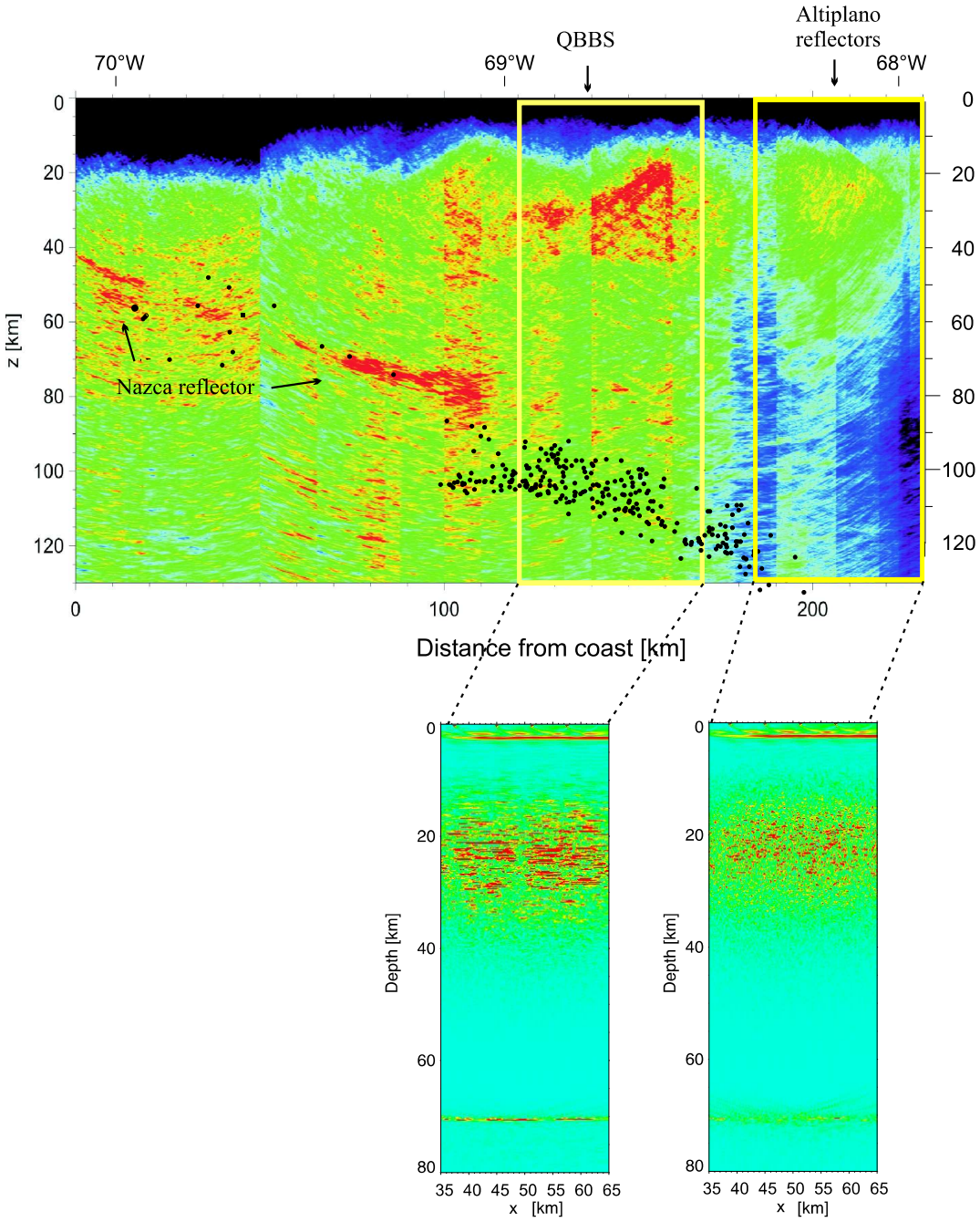

Figure 3.8: Comparison of synthetic depth sections with the ANCORP image. The modelling results suggest that the apparent breakdown of the reflectivity between 110 - 160 km at depths larger than 80 km is due to scattering in the QBBS (compare left yellow box with lower left section). The synthetic results also indicate that a complex zone of heterogeneities with strong velocity fluctuations and correlation lengths in the order of few hundred meters cause the complete loss of the reflectivity of the deeper region (compare the right yellow box with lower right section). The Altiplano reflectors represent such a zone.

However, the results of the numerical modelling indicate that the abrupt change in reflectivity might be also connected with the presence of a strongly heterogeneous layer above the Nazca reflector. A heterogeneous layer with horizontal correlation lengths of few kilometers and a standard deviation of the velocity fluctuation of 10 % might cause the apparently weak reflectivity of the Nazca reflector. The QBBS represents such a heterogeneous layer. The QBBS is a high reflective zone showing short and incoherent internal reflections. Strong multiple scattering within this zone is assumed to cause the observed high reflectivity and a strong attenuation of the transmitted field. Consequently, the reflectivity of the Nazca reflector is significantly decreased. The lack of deep reflections in the eastern part of the profile (185 - 230 km) is also related to the presence of a heterogeneous layer in the overburden. Here, it is assumed that the magnitude of the velocity fluctuations is higher and that the correlation lengths of the heterogeneities are in the order of the wavelength, but small compared to the Fresnel zone width. Thus, the estimated horizontal correlation length of the heterogeneities within the Altiplano subsurface is few hundred meters. This would provide the diffuse reflections observed for the Altiplano reflectors. It is concluded that the apparent reflectivity decrease of the Nazca reflector is not only caused by petrological changes, but also by the strong scattering in the heterogeneous structures above.

3.2.2 Reflection Image Spectroscopy - RIS

The Reflection Image Spectroscopy method RIS was invented to extract structural details from seismic reflection images of strongly heterogeneous media. The method accounts for the frequency dependence of scattering. Scattering is regarded as the redistribution of seismic energy into reflected (backscattered) and transmitted (forward scattered) waves. The amount of the scattered energy and of the wave field fluctuations varies in dependence on the magnitude of the velocity fluctuation as well as on the ratio between the wavelength and the spatial size of the heterogeneities. Therefore, seismic images will significantly differ when migration is performed focusing on different frequency ranges. Strong scattering in a certain frequency-band of the data will lead to severe amplitude loss and phase fluctuation. The image of a deep reflector will be affected by the loss of coherency and reflection strength. The reflector shape will be biased or the reflector is screend at all. In comparison to the latter scattering in another frequency band might be less severe, such that reflectors are imaged with properly or at least less biased reflectivity and shape. In the broadband image the fluctuations are superposed, covering the coherent reflections. Besides the extraction of the undistorted reflectors the method is furthermore applied to

gain additional information on the spatial parameters of the heterogeneities in the medium.

The proceeding of the method is the following. The seismogram sections are filtered in different frequency bands. The filtered data are then processed and imaged according to the usual scheme. The resulting depth sections are compared and analysed qualitatively to reveal potentially covered reflectors and the undistorted real geometries of deep reflectors. A quantitive analysis of the reflectivity in dependence on the frequency content of the depth sections provides insights on the internal structure of the heterogeneous layer.

Here, the analysis focused on the appearance of the deep reflector in dependence on the imaged frequencies. A profound analysis of the reflectivity in the heterogeneous layer in connection with the extraction of spatial parameters of the heterogeneities, i.e. correlation lengths, will be the subject of future work.

Model and data set-up

The RIS method was applied to a set of five synthetic seismogram sections. The seismogram sections were calculated for the velocity model with 5 % standard deviation and a horizontal correlation length of $a_x = 1000$ m. This model was already introduced in subsection 3.2.1. Three low-pass filters and 4 band-pass filters were applied to the data. The frequency bandwidth of the low-pass filters varied between 5 - 15 Hz. The lower cut-off frequency was kept constant at 0 Hz. The upper cut-off frequency was continuously shifted to lower frequencies. The frequency range of the low-pass filters were 0 - 20 Hz, 0 - 15 Hz, and 0 - 10 Hz. The spectra of the low-pass filtered traces are shown in the left column of Fig. 3.9 [(2) - (4)]. The spectrum of the unfiltered trace is shown in (1) of Fig. 3.9. The frequency band width of the band-pass filters was kept constant to 5 Hz. Four filters with the central frequency band between 0 - 5 Hz, 5 - 10 Hz, 10 - 15 Hz, and 15 - 20 Hz were applied to the seismogram sections. The spectra of the band-pass filtered traces are shown in the right column of Fig. 3.9 [(5) - (8)].

After the frequency filtering the seismogram sections were migrated. The final depth sections were obtained by stacking the migrated single depth sections. The results are presented in the following.

Results

In Fig. 3.10 the low-pass filtered depth sections are shown. The amplitude scaling is the same in all images. Migration of unsuppressed first arrivals caused the strong reflections

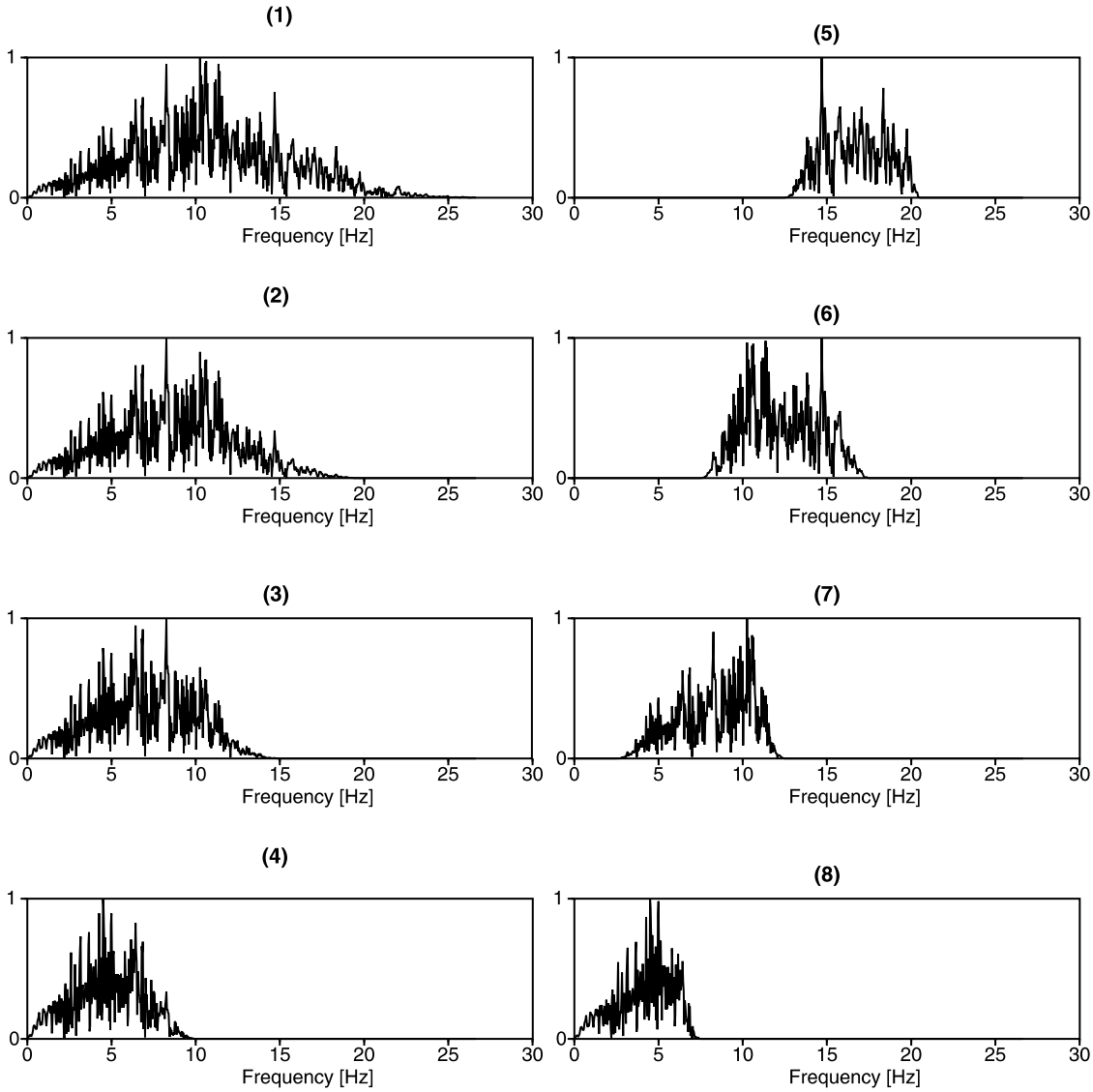

Figure 3.9: Normalised amplitude spectra of unfiltered and filtered traces. (1): Unfiltered frequency spectrum. (2) - (4): Amplitude spectra of low-pass filtered traces. (5) - (8): Amplitude spectra of band-pass filtered traces.

visible at depths between 3 - 5 km. The frequency bands of the depth sections correspond to the frequency spectra shown in Fig. 3.9 (left column). The recalculated images are shown for the unfiltered data, and for frequencies between 0 - 20 Hz, 0 - 15 Hz, and 0 - 10 Hz. The minimum wavelength in the data is $\lambda \approx 240\ m$ for 10 Hz in the unfiltered section, and $\lambda \approx 600\ m$ for 10 Hz in the low-frequency section. The widths of the normal-incidence Fresnel zone at a depth of 20 km are $W_{Fr} \approx 3100\ m$ and $W_{Fr} \approx 4900\ m$, respectively. In the unfiltered image reflections from the heterogeneous layer appear complex revealing short and longer scale structural details. When filtering the high-frequency components from the data the reflections become smooth. Short wavelengths details are continuously removed. The deep reflector in the unfiltered depth image appears disrupted and incoherent. The real shape is not recognisable. The reflector becomes more coherent and less distorted when the high frequency contents are filtered out. In the 0 - 10 Hz depth section the reflector appears coherent and clear.

Fig. 3.11 shows the band-pass filtered depth sections. The frequency bands range between 15 - 20 Hz, 10 - 15 Hz, 5 - 10 Hz, and 0 - 5 Hz (see also Fig. 3.9, right column). In the band-pass filtered depth sections the contributions from different frequency ranges to the reflection image are separated. In the 15 - 20 Hz and the 10 - 15 Hz image very short and diffusive reflection patterns with comparably weak reflectivity are visible in the heterogeneous layer. The reflections become apparently horizontally layered in the 5 - 10 Hz and 0 - 5 Hz depth sections. The deep reflector in the high frequency image (15 - 20 Hz) appears discontinuous and incoherent. The distortion of the reflector shape is severe. In the 10 - 15 Hz section the reflector appears less distorted and more coherent. The coherency increases in the low-frequency images. In the 0 - 5 Hz section a clear and coherent image of a plane reflector is recovered.

The results show that the reflection images differ when imaging only narrow frequency bands of the data. Especially the image fluctuations for structures below the heterogeneous layer can be severe in one frequency band, when amplitude and phase fluctuation due to scattering are stronger than in another frequency band. In the broadband image these fluctuations are superposed on the less or non-fluctuating reflections and cover the real shape of reflectors and bias the reflectivity. However, by processing the data in narrow frequency bands the undistorted reflector can be recovered.

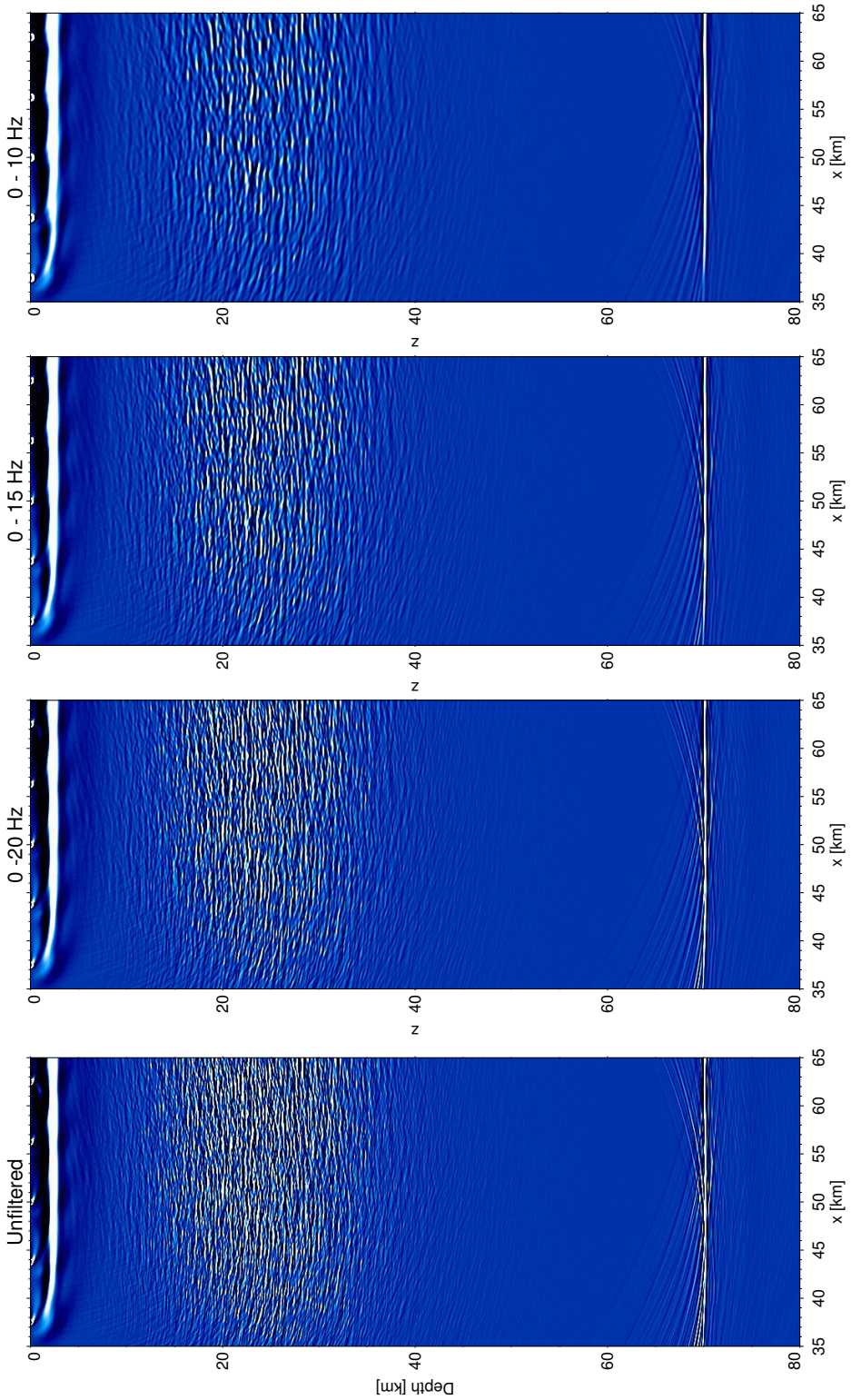

Figure 3.10: Low-pass filtered depth sections. The reflectivity in the heterogeneous layer becomes weak and smooth with continuous removal of the high frequency contents. In the unfiltered section the deep reflector appears disrupted and incoherent. The reflector becomes sharp and clear, when high frequencies are filtered from the data.

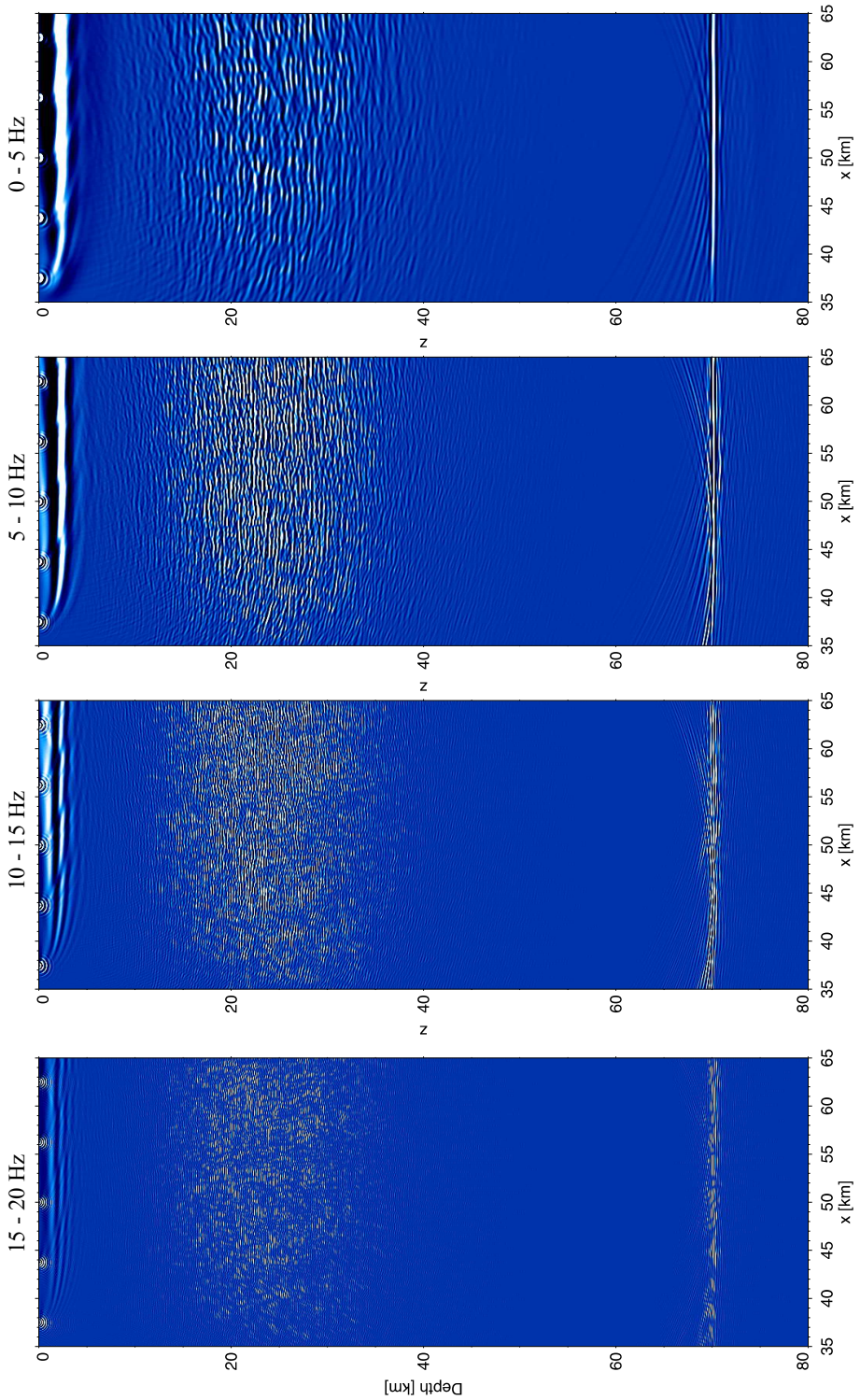

Figure 3.11: Band-pass filtered depth sections. The deep reflector in the high frequency image is severely affected coherency loss (15 - 20 Hz), whereas in the low frequency image the reflector is clear and undistorted (0 - 5 Hz).

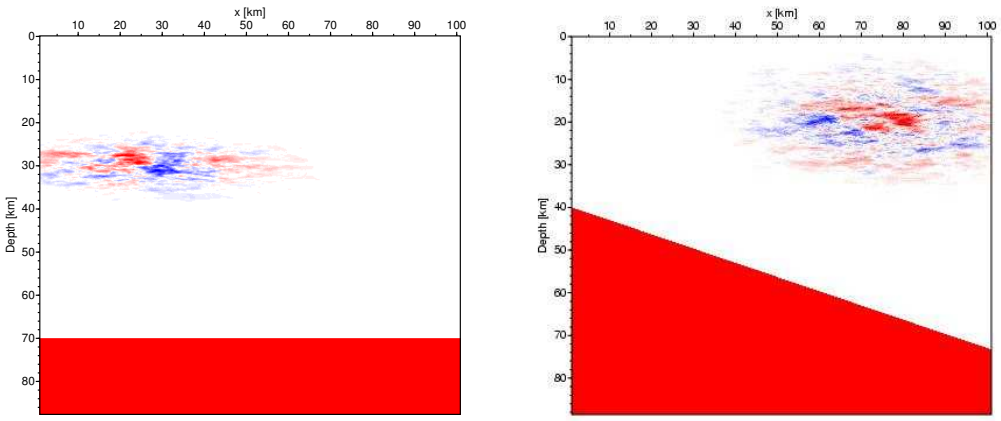

(a) (b)

Figure 3.12: The velocity models. (a) Velocity model with a deep horizontal reflector beneath a 10 km thick heterogeneous layer. (b) Velocity model with a dipping reflector and a 20 km thick heterogeneous layer. In both models the background velocity of the upper part is $v_P = 6000$ ms^{-1}, the standard deviation is 15 %, and the correlation lengths are $a_z = 1000$ m and $a_x = 5000$ m. The velocity fluctuations were tapered exponentially in the horizontal and vertical direction.

3.2.3 Impact of the velocity model on migration

Excellent velocity control during the migration process is an important factor in seismic imaging. In the following the influence of migration velocity errors on the coherency and the shape of reflectors will be analysed.

Model and data set-up

To study the effect of migration velocity on the seismic image two velocity models were generated (Fig. 3.12. The first model consists of a horizontal deep reflector below a 10 km thick heterogeneous layer, the second model of a dipping reflector beneath a heterogeneous layer with a thickness of 20 km. The background velocity of the upper part is $v_P = 6000$ ms^{-1} in both models. The velocity of the lower layer was $v_P = 8000$ ms^{-1}. The v_P/v_S ratio was set to $\sqrt{3}$. The densities were calculated after the empirical Nafe-Drake relation (see section 3.2.1). The standard deviation of the velocity fluctuations was 15 %

in both models. The horizontal and the vertical correlation lengths were set $a_x = 5000$ m and $a_z = 5000$ m, respectively. The fluctuation field was exponentially tapered in the vertical direction (eq. (3.5), see section 3.2.1). The tapering function was also applied in the horizontal direction. This was done to directly study the change of coherency along the deep reflector in connection with the overburden.

14 split-spread shot gathers were calculated for each model. The shot and receiver lines introduced in section 3.2.1 were extended by two recording lines located between 31.25 km - 56 km and 25 km - 50 km. Two shot gathers with the source points located on either side were recorded for each receiver line. This increased the aperture and the data coverage. Three different migration velocities were used, i.e. the real background velocity ($v = 6000$ ms^{-1}), a velocity which was 5 % faster than the true velocity ($v = 6300$ ms^{-1}), and one which was 5 % slower ($v = 5700$ ms^{-1}). The final depth sections were obtained by stacking of the migrated single sections and are presented in the following.

Results

The depth sections calculated for the horizontal reflector model are shown in Fig. 3.13. The migration velocity was $v = 5700$ ms^{-1} in the left section (section 1), $v = 6000$ ms^{-1} in the middle (section 2), and $v = 6300$ ms^{-1} in the right section (section 3). The images are displayed with the same amplitude scaling.

The heterogeneous layer appears at similar depths between 25 - 35 km in all sections. In section 1 the heterogeneous layer is very slightly upward shifted, whereas in section 3 it is slightly shifted down in depth. The thickness of the heterogeneous layer in section 1 and section 3 appears slightly less compared to the observed thickness in section 2. The horizontal reflector looks similar in all sections. In the right part of each section the reflector appears sharp and coherent. In the middle of the section, where the heterogeneous layer appears, the coherency of the reflector decreases slightly. Towards the left part of the section the reflector increasingly appears incoherent and weak. The depth of the reflector changes when using different migration velocities. The real depth of the reflector is 70 km. The depth of the reflector are ~ 67 km and ~ 73.5 km when the migration velocity were $v = 5700$ ms^{-1} and $v = 6300$ ms^{-1}, respectively.

Similar results were obtained for the dipping reflector model (Fig. 3.14). The depth sections are shown for a migration velocity of $v = 5700$ ms^{-1} on the left (section 4), $v = 6000$ ms^{-1} in the middle (section 5), and $v = 6300$ ms^{-1} on the right (section 6). As observed before the reflector looks similar in all sections. The reflector appears coherent

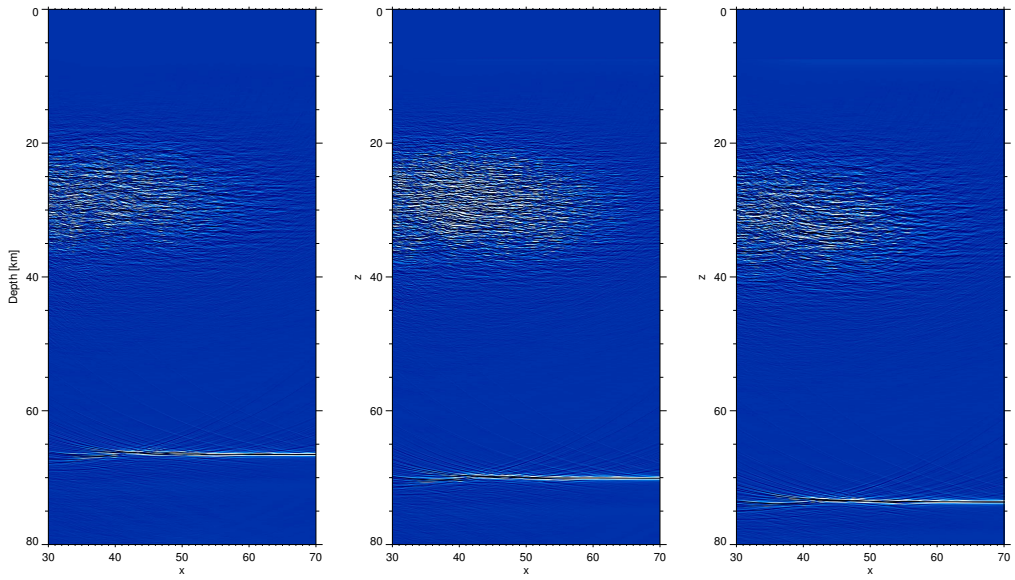

Figure 3.13: Depth sections with a horizontal reflector calculated for different migration velocities. The migration velocities were $v = 5700$ ms^{-1} (left), $v = 6000$ ms^{-1} (middle), and $v = 6300$ ms^{-1} (right).

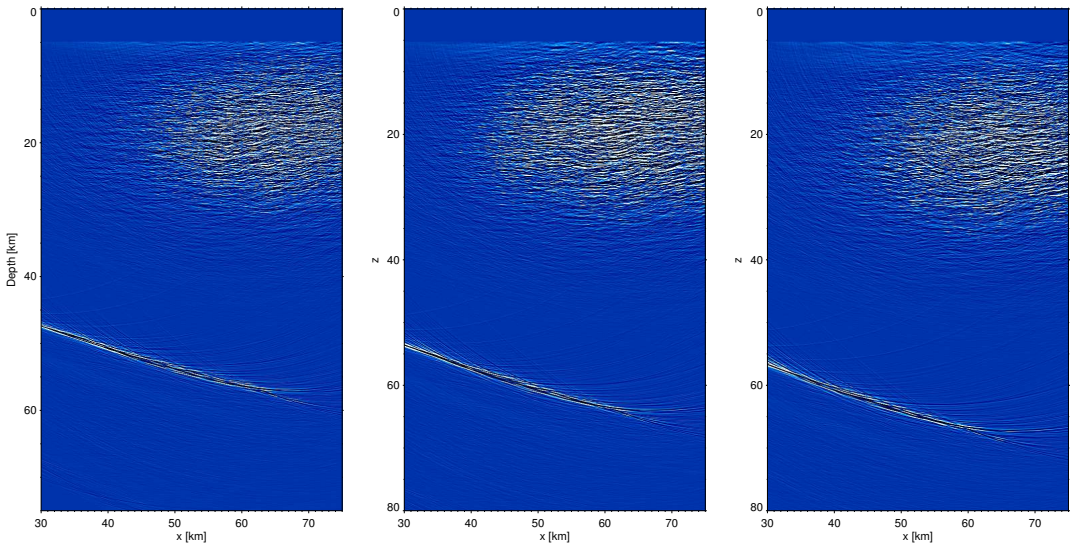

Figure 3.14: Depth sections with a dipping reflector calculated for different migration velocities. The migration velocities were $v = 5700$ ms^{-1} (left), $v = 6000$ ms^{-1} (middle), and $v = 6300$ ms^{-1} (right).

in the left part and becomes incoherent below the heterogeneous layer in the right part of the section. Migration using a wrong velocity changes the depth of the dipping reflector. In section 4 the depth of the dipping reflector at $x = 30$ km is ~ 47.5 km depth. The reflector depth at the same position is $\sim$57 km section 6. The real depth of the reflector is 53 km (section 5). The shift of the reflector is slightly larger for the dipping reflector than for the horizontal reflector. Similar to the previous observation the results show that mainly the depth of the reflector is affected by using wrong migration velocities. The coherency and the shape of the reflector are not influenced.

In summary it can be noted that the coherency of the reflector located below a heterogeneous layer is not affected when wrong migration velocities are used. Only the depth of the reflector is affected. To reveal whether the coherency loss of the reflector is more severe due to errors in laterally varying velocity models further numerical modelling studies seem to be necessary.

3.3 Summary and conclusion

In this chapter seismic images in the presence of weak and strongly scattering heterogeneous layers were studied focusing on three aspects:

1. Influence of a heterogeneous layer on the reflectivity and coherency of reflections.

2. Frequency dependent reflection images (RIS).

3. Effect of errors in the velocity model on the reflector.

For this purpose numerical modelling experiments using FD modelling and Kirchhoff prestack depth migration were carried out. Synthetic depth sections were calculated for velocity models with varying magnitude of velocity fluctuations and correlation lengths of the heterogeneous layer therein.

The results from the first experiment show that the reflectivity in a heterogeneous layer increases when velocity fluctuations become strong. For the same standard deviation the average reflectivity in the heterogeneous layer is stronger for large correlation lengths than for smaller correlation lengths. The same holds for the reflectivity of the deep reflector. Considering the same standard deviation, then the reflectivity is weak for small correlation lengths compared to the reflectivity observed for large correlation lengths. The amount of scattered energy is not only dependent on the magnitude of the velocity fluctuation, but also on the ratio between the wavelength and the correlation length.

The comparison of the numerical modelling results with the ANCORP image indicates that the abrupt change in reflectivity at depths larger than 80 km and the lack of deeper reflections in the eastern part of the profile might be related to the presence of a strongly heterogeneous layer above. The QBBS and the Altiplano reflectors represent such heterogeneous layers. It is assumed that the correlation lengths of the heterogeneities in the QBBS are few kilometers, and in the Altiplano region few hundred meters. These numbers correlate with the observed reflection pattern of both structures.

The RIS method applied to synthetic data shows that the reflections differ when imaging only narrow frequency bands of the data. The image fluctuation of a reflector below a heterogeneous layer is severe in one frequency band and less another frequency band. The reflector appears discontinuous and disrupted when scattering is strong, and clear and coherent when scattering becomes weak. In the broadband range these fluctuations are superposed on the less or non-fluctuating part and cover the real shape of the reflector. The RIS method shows that the analysis of narrow frequency band images is able to extract the undistorted real reflector. Thus, in real data application the method can significantly improve the structural interpretation.

The last study investigated the influence of the velocity model errors on the reflector. The results show that the shape and the coherency of the reflector are not influenced. Only the depth of the reflector is affected. The depth shift is slightly larger for dipping reflectors than for horizontal reflectors. However, further numerical modelling studies seem to be necessary to reveal whether the coherency loss of the reflector is more severe in the case of errors of laterally varying velocity models.